Modelling and Dynamic Analysis of Rotor-AMBs System with Shrink Fit Assembly

Yang ZHOU [a], Jin ZHOU [a], Jarir MAHFOUD [b], Yuanping XU [a]

a Nanjing University of Aeronautics and Astronautics, Yudao Street 29, 210016 Nanjing, China, zhouyang0216@nuaa.edu.cn

b University of Lyon, INSA-Lyon, CNRS UMR5259, LaMCoS, F-69621 Villeurbanne Cedex, France

Abstract

Rotor-active magnetic bearings (rotor-AMBs) systems nowadays have been widely used in fluid machinery and the shrink fit assembly is widely applied in the rotor. However, when the shrink fit is tight enough, additional external perturbation could be introduced when rotor is levitated. The mechanism of this additional perturbation should be assessed to ensure stable operation of the machine. The effect of the shrink fit interface contact is equated to an additional stiffness matrix by massless spring units, whose certain contact stiffness is uniformly distributed over the interface. Particularly, we consider that there is partial separation in the contact interface due to the AMBs supporting and a novel additional stiffness matrix related to contact status is proposed by calculating the real-time contact area. The contact stiffness is calculated by microscopic contact model based on fractal theory. Finally, numerical simulation shows that the interface contact influences the system robustness and the unstable mode is excited. The increase of interference and contact length both will increase the amplitude of the rotor response. Moreover, the influence and order of the vibration are quantitatively validated by the experiments.

Keywords: Active Magnetic Bearing, shrink fit, interface contact, flexible mode vibration

1. Introduction

Active magnetic bearings (AMBs) have been widely used in centrifugal gas compressors and other high-speed fluid machinery applications (Schweitzer and Maslen, 2009). In these rotating machinery, mechanical elements such as disks and impellers are often shrink fitted on the shafts, and the shrink fit assembly forms the interface contact. However, when the connection is tight enough, the flexible mode vibrations will be excited when rotor is levitated. However, when the shrink fit interference decreases, the rotor can be levitated stably. To sum up, the cause of this vibration is the coupling between the assembly interface contact and the AMB supporting, of which few studies have been studied.

Shrink fit assembly is widely applied in rotor – bearing system. Unlike the traditional complete rotor, the presence of the interface contact may bring changes to the dynamic characteristic of rotor. Tan et al. equated the rotor shrink-fit interface to an internal damping force and analyzed its influence on system stability by decomposing the asymmetric stiffness component from the system equations (Tan, et al., 2014). Francesco Sorge studied the internal friction in the rotor – shaft system due to the shrink fit release of the assembly (Sorge, 2013a, 2014b). The internal friction tends to destabilize the over-critical rotor running. The friction works between two rotating parts. The internal friction between rotating parts produces a destabilizing force in the following way (Yukio and Toshio, 2012). When a deflected elastic shaft whirls with an angular velocity that differs from the rotational speed, the fibers of the shaft elongate or contract in the hub. A fiber on the shaft surface contracts while it moves from the outside to the inside of the orbit circle and elongates while it moves from the inside to the outside. Then, dry friction works from the hub to the shaft surface to prevent this motion. However, this vibration mechanism is not able to interpret the flexible mode vibration caused by shrink fit interface contact in AMBs-suspended machinery due to: 1. The rotor with shrink fit assembly is levitated by AMBs; 2. This vibration is excited without rotation.

Yannick Paul et al. mentioned that the poor connection between rotor and the impeller may cause high-frequency vibration during levitation in the expander-compressors with AMBs (Smithanik and Yannick, 2015). Wei and Fang equated the influence of shrinkage fit in a rigid rotor to a disturbance in the rotational direction (Wei and Fang, 2008). Simon and Flowers equated the shrink fit contact effect to an internal damping force and analyzed its influence on the rotor-AMB system stability when rotating (Andras and Flowers, 2007a, 2009b). It can be seen in these results that the interface contact significantly influences the system stability. We also note that these results are all based on excitation of the unbalance force and the internal damping force, but not the contact effect. However, contact effect plays a significant role in amplifying the excitation, which leads to system instability. In AMB suspended rotating machinery, the energy input from the AMB supporting is seen as the excitation and is amplified by the contact effect.

In traditional modeling of the rotor assembled by several components with shrink fit, the Young's modulus and density of lamination stacks are updated based on the experimental identification of natural frequencies (Xu, et al., 2015). This method focuses on the natural frequencies of the rotor and ensures the modeling accuracy. However, this approach should consider the contact characteristics due to the shrink fit. This paper proposed a new modeling of the rotor-AMBs System with shrink fit assembly. The effect of the interface contact is equivalent to an additional stiffness matrix by simplifying the interface contact to massless spring units, whose certain contact stiffness is uniformly distributed over the contact interface. The dynamic response of the rotor supported by AMBs considering the effect of shrink fit interface contact is studied by numerical simulation in this paper.

2. Modelling of rotor-AMBs system with shrink fit

2.1 Description of the rotor – AMBs test rig

The four-degree of freedom rotor-AMBs experimental test rig shown in Fig. 1 for this study consists of two parts: the mechanical system and the electronic control system. The rotor supported by the radial AMBs A and B has a length of 1.004 m and a weight of 10.35 kg. A disk connected to the rotor by shrink fit on the right end to simulate the influence of interface contact. Disks of different inner diameters and axial lengths are manufactured to simulate the effect of interference and contact length on system's response.
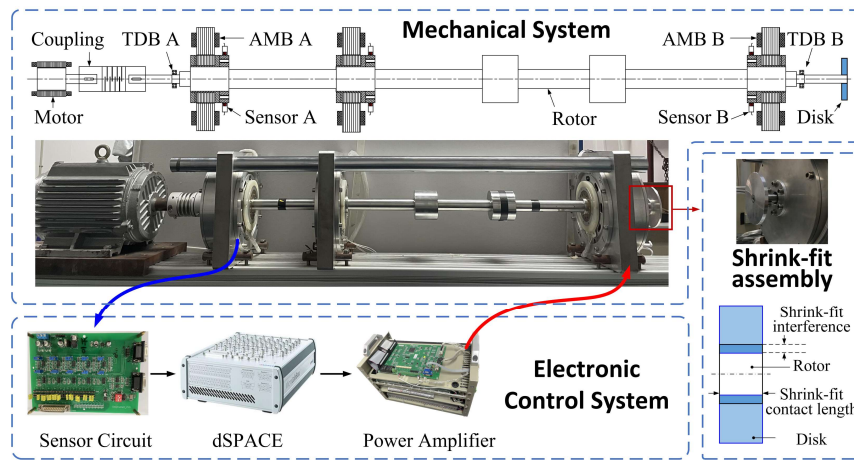
Figure 1   Rotor-AMBs test rig.

2.2 Modelling of the interface contact

This work focuses on the influence of the shrink fit interface on the rotor. The interface contact in the rotor is modeled as a uniformly distributed stiffness over the contact interface as shown in Fig. 2(a), where the disk and the rotor are joined together by shrink fit assembly. The arbitrary node i_s on the outer surface of rotor is connected to its corresponding node j_s by the spring unit. The stiffness of the massless spring unit is referred to as the contact stiffness. The contact stiffness can be subdivided into the normal contact stiffness k_f and the tangential contact stiffness k_q. The directions of k_f and k_q are perpendicular and parallel to the contact interface, respectively. The value of the contact stiffness is related to the interference δ and the contact area A_a ($A_a=2\pi RL$). There is relative deformation between the contact interfaces when the rotor vibrates. The energy generated by the spring deformation is calculated to study the influence of the interface contact. According to the energy principle of the spring unit, the energy of the unit spring Δu can be obtained by the linear superposition of the change of the spring potential energy in the x, y and z directions as,

$$\Delta u = \Delta u_x + \Delta u_y + \Delta u_z = 0.5 \cdot k_q \Delta x^2 + 0.5 \cdot k_q \Delta y^2 + 0.5 \cdot k_f \Delta z^2 \tag{1}$$

where Δx, Δy and Δz represent the deformation of each spring unit in the x, y and z directions, respectively.

In the shrink fit assembly, the center node of the rotor is node i and the center node of the disk is node j. The generalized coordinates of centers i and j are $(x_i,y_i,\alpha_i,\beta_i)$ and $(x_j,y_j,\alpha_j,\beta_j)$, respectively in absolute coordinates $oxyz$. As shown in Fig. 2(b). By establishing the floating coordinate of node i and j, the coordinates of node i_s can be expressed as in the absolute coordinate system $oxyz$ as

$$\begin{cases} x_{is} = x_i + l\sin\alpha_i\cos\beta_i - R\cos\theta\cos\beta_i \\ y_{is} = y_i + l\sin\beta_i + r\cos\theta\sin\beta_i\sin\alpha_i + r\sin\theta\cos\alpha_i \\ z_{is} = z_i + l\cos\alpha_i\cos\beta_i - r\cos\theta\sin\beta_i\cos\alpha_i + r\sin\theta\sin\alpha_i \end{cases} \tag{2}$$

The coordinates of node j_s can be obtained using this method.

(a)

(b)
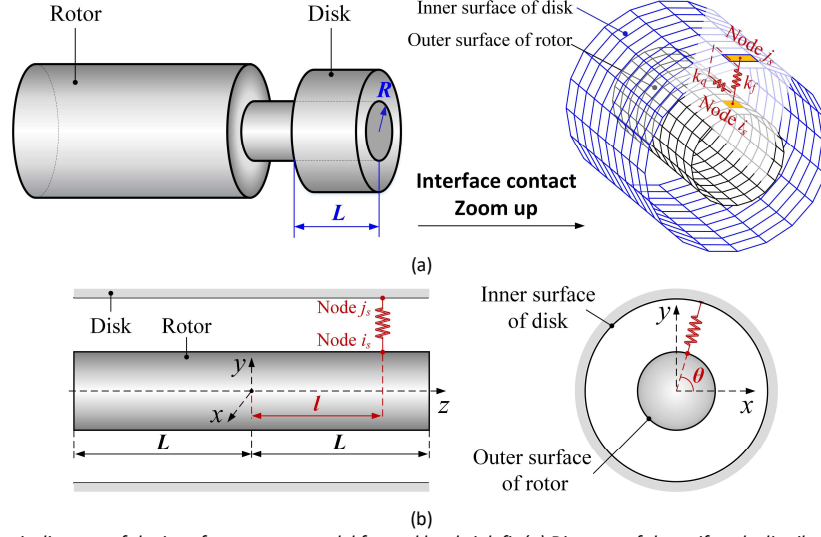
Figure 2   *Schematic diagram of the interface contact model formed by shrink fit (a) Diagram of the uniformly distributed spring unit (b) The coordinate of the spring unit.*

The deformation of the spring unit Δx, Δy and Δz in the absolute coordinate system is calculated by the coordinates of i_s and j_s as,

$$\begin{cases} \Delta x = x_{js} - x_{is} = x_j - x_i + l\left(\alpha_j - \alpha_i\right) \\ \Delta y = y_{js} - y_{is} = y_j - y_i + l\left(\beta_j - \beta_i\right) \\ \Delta z = z_{js} - z_{is} = R\sin\theta\left(\alpha_j - \alpha_i\right) + R\cos\theta\left(\beta_i - \beta_j\right) \end{cases} \quad (3)$$

The total energy generated by the spring unit is obtained by summing up the unit spring energy Δu as follows

$$\begin{aligned} u_s &= \iint_A 0.5\left(k_f\Delta x^2 + k_f\Delta y^2 + k_q\Delta z^2\right)\mathrm{d}A \\ &= \int_{-L}^{L}\int_0^{2\pi} 0.5\left(k_f\Delta x^2 + k_f\Delta y^2 + k_q\Delta z^2\right)\mathrm{d}\theta\mathrm{d}l \end{aligned} \quad (4)$$

where A denotes the contact region and the area of A is given by $A_a = 2\pi RL$ when the two interfaces are fully contacted (Wu, et al., 2021). However, the rotor and disk interfaces are not fully contacted when the rotor is levitated. It is assumed that the contact interface is partly separated as shown in Fig. 3(a). The orange and the blue line are the Intersecting lines formed by the intersection of the outer surface of the rotor and the inner surface of the disk. In the Fig. 3(b), we expand the rotor outer surface along the circumferential direction, it can be seen that the real contact region is enclosed by the blue line $z_1(\theta)$ and the red dotted line $z_2(\theta)$, which is colored.

(a)

(b)
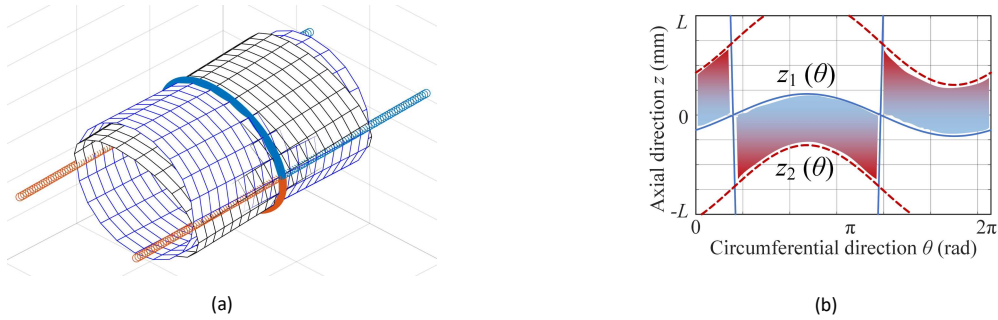
Figure 3   *Schematic diagram of the actual contact status between the rotor and the disk (a) Diagram of the partly separation in 3D view (b) The expansion of the rotor outer surface along the circumferential direction.*

For $z_1(\theta)$ and $z_2(\theta)$, the blue and the red line are obtained by deriving the intersecting line equation of the two cylindrical surfaces. The function of $z_1(\theta)$ and $z_2(\theta)$ change with the generalized coordinates of nodes i and j. Therefore, the total energy is time-variant and can be expressed as

$$u_s = \int_{z_1(\theta)}^{z_2(\theta)}\int_0^{2\pi} 0.5\left(k_f\Delta x^2 + k_f\Delta y^2 + k_q\Delta z^2\right)\mathrm{d}\theta\mathrm{d}l \quad (5)$$

Submitting Eq. (4) into Eq. (6), we can express the total elastic potential energy u_s as

$$u_s = 0.5 \cdot \begin{bmatrix} x_i & y_i & \alpha_i & \beta_i & x_j & y_j & \alpha_j & \beta_j \end{bmatrix} K_e \begin{bmatrix} x_i & y_i & \alpha_i & \beta_i & x_j & y_j & \alpha_j & \beta_j \end{bmatrix}^{\mathrm{T}} \tag{6}$$

$$K_e = \begin{bmatrix} \mathrm{diag}\left(k_q \iint_A dA, k_q \iint_A dA, k_f \iint_A y^2 dA, k_f \iint_A x^2 dA\right) & -\mathrm{diag}\left(k_q \iint_A dA, k_q \iint_A dA, k_f \iint_A y^2 dA, k_f \iint_A x^2 dA\right) \\ -\mathrm{diag}\left(k_q \iint_A dA, k_q \iint_A dA, k_f \iint_A y^2 dA, k_f \iint_A x^2 dA\right) & \mathrm{diag}\left(k_q \iint_A dA, k_q \iint_A dA, k_f \iint_A y^2 dA, k_f \iint_A x^2 dA\right) \end{bmatrix} \tag{7}$$

The time-variant additional stiffness matrix K_e arising from the interface contact will be added to the dynamic equations of the system as the influence of the interface contact. The main contact effect variables are the normal contact stiffness k_f, tangential contact stiffness k_q and the contact length L.

The contact stiffness model of shrink-fit interface is established based on the elastic-plastic contact model and fractal theory (Liu, et al., 2019). The microscopic contact model of the annulus can be simplified to the microscopic contact model of the planes. Considering that the nominal radius R of shrink fit is fixed, the normal contact stiffness and tangential contact stiffness under different interference and contact length L is shown below.

(a)   (b)
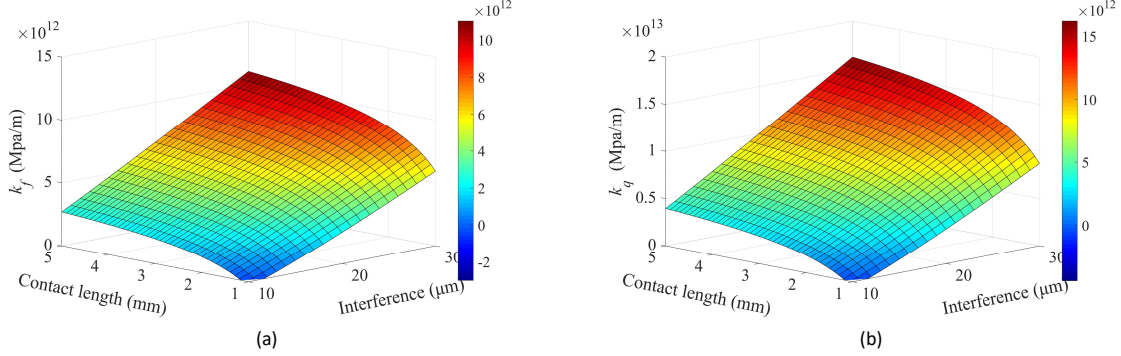
Figure 4   Calculation of the normal stiffness and tangential stiffness of the shrink fit (a) Normal stiffness under different interference δ and different contact length L (b) Tangential stiffness under different interference δ and different contact length L.

2.3 Modelling of the rotor-AMBs system

The theory of Bernoulli-Euler beam is applied to the finite element of the rotor. The rotor is modelled with 66 nodes and 64 elements for a total mesh of 264 DOF for the lateral analysis (see Fig. 5). The equation of motion takes the following form.

$$M_R \ddot{q} + C_R \dot{q} + K_R q = 0 \tag{8}$$

where M_R, C_R and K_R represents the mass matrix, the damping matrix and the stiffness matrix of the system, respectively. F_{AMB} represents the electromagnetic force by the AMBs. Vector q represents the system displacement vector $[x_1, y_1, \alpha_1, \beta_1 \ldots x_{66}, y_{66}, \alpha_{66}, \beta_{66}]^T$, where the generalized coordinates of centers i and j are also included.
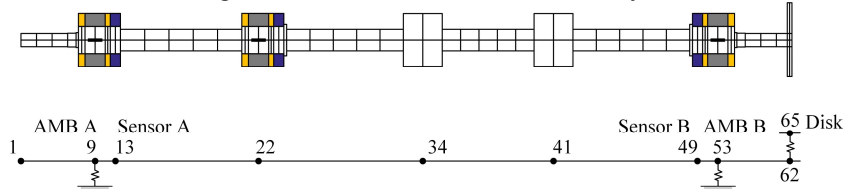
Figure 5   The finite element model for the rotor-AMBs system with shrink fit.

The active magnetic bearing generates the attractive force in differential driving mode, and the electromagnetic force f_{amb} is linearized and expressed as

$$f_{amb} = k_x x + k_i i \tag{9}$$

where k_x and k_i represent the displacement stiffness and the current stiffness, respectively.

Substituting Eq. (8) and Eq. (10) into Eq. (9), the general equation of motion could be written as

$$M_R \ddot{q} + C_R \dot{q} + \left(K_R - T_e^{\mathrm{T}} K_e T_e\right) q = k_x T_a^{\mathrm{T}} T_a q + k_i T_a^{\mathrm{T}} i_a \tag{10}$$

where T_e is the transfer matrix of the interface nodes i and j, T_a is the transfer matrix of the AMB nodes, i_a is the control current of AMBs A and B in the x and y directions.

The state space model of the rotor-AMBs system considering the interface contact can be expressed as

$$\begin{cases} \dot{x}_s = \begin{bmatrix} \dot{q} \\ \ddot{q} \end{bmatrix} = \begin{bmatrix} 0 & I \\ -M_R^{-1}\left(K_R - k_x T_a^{\mathrm{T}} T_a - T_e^{\mathrm{T}} K_e T_e\right) & -M_R^{-1} C_R \end{bmatrix} \begin{bmatrix} q \\ \dot{q} \end{bmatrix} + \begin{bmatrix} 0 \\ k_i M_R^{-1} T_a^{\mathrm{T}} \end{bmatrix} i_a = A_s x_s + B_s i_a \\ q_s = \begin{bmatrix} q_{sAx} & q_{sAy} & q_{sBx} & q_{sBy} \end{bmatrix}^{\mathrm{T}} = \begin{bmatrix} T_s & 0 \end{bmatrix} \begin{bmatrix} q & \dot{q} \end{bmatrix}^{\mathrm{T}} = C_s x_s \end{cases} \tag{11}$$

where x_s is the state vector, q_s is the displacement of the sensor nodes in the x and y directions, and T_s is the transfer matrix of the sensor nodes.
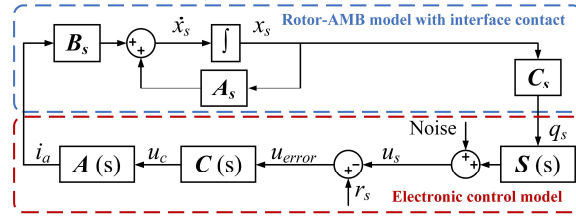
Figure 6   Diagram of the closed-loop mathematical model considering interface contact.

As shown in Fig. 6, beside modelling the rotor and the electromagnetic forces, modelling of the electronic control system, which consists of the eddy-current sensors, the amplifiers and the controllers, is also needed.

The relationship between the control currents and the radial rotor displacement q_s detected by the sensors is given as Eq. (13)

$$i_a = \frac{i_a}{u_c}\frac{u_c}{u_{error}}(r_s - u_s) = A(s)C(s)\left[r_s - S(s)q_s\right] = \frac{k_a(2\pi f_z)}{s+(2\pi f_z)}\cdot\left(K_P + \frac{K_I}{s} + \frac{K_D s}{T_D s + 1}\right)(r_s - k_s q_s) \tag{12}$$

where $S(s)$, $A(s)$ and $C(s)$ are the transfer functions of the sensor, the amplifier and the controller, respectively, k_s is the gain of sensor, k_a is the gain of power amplifier, f_z is the cut-off frequency, K_P, K_I and K_D respectively represent the proportional gain, the integral gain, the derivative gain, T_D is the derivative time constant to prevent magnifying the error signal by the controller in the high frequency ranges, and r_s is the reference voltage.

As shown in Fig. 6, the rotor-AMBs mechatronic system considering interface contact is established by combining the rotor-AMBs model considering interface contact and the electronic control model.

3. Numerical simulation

The dynamic response of the rotor supported by AMBs considering the effect of shrink fit interface contact is studied by using numerical simulation in this paper.

In order to study the influence of the interface contact on the system, appropriate control parameters should be tuned to ensure stable levitation of the rotor without interface contact. In order to simplify the model and increase the calculation speed, only the first five bending modes are retained through model reduction. The parameters in the PID controller in simulation are given as: K_P =1.7, K_I =1, K_D =0.0006, T_D =0.0001. In this work, these parameters are kept the same to exclude the influence of the controller.

When L is 3 mm, the influence of the shrink fit interference on the rotor displacement is shown in Fig. 7. Varying the value of the interference from 5 μm to 15 μm, the time domain response plotted in Fig. 7(a) shows that, as L increases, the amplitude of the response increases, and as L increases, the vibration appears faster, which means that the system is more unstable. By comparing the rotor responses at the positions of AMB A and AMB B, the response near the disk (the B_x direction) is greater than the response of the other side (the A_x direction). In the frequency domain, it can be seen in Fig. 7(b) that the rotor vibrates around the 4th bending mode frequency.

When δ is 10 μm, the influence of the contact length on the rotor displacement is shown in Fig. 8. Varying the contact length from 2 mm to 4 mm, the time domain response plotted in Fig. 8(a) shows that, as L increases, the amplitude of the response also increases. Similarly, response near the disk is greater than the response of the other side. In the frequency domain, it can be seen in Fig. 8(b) that the rotor vibrates around the 4th bending mode frequency.

(a)   (b)
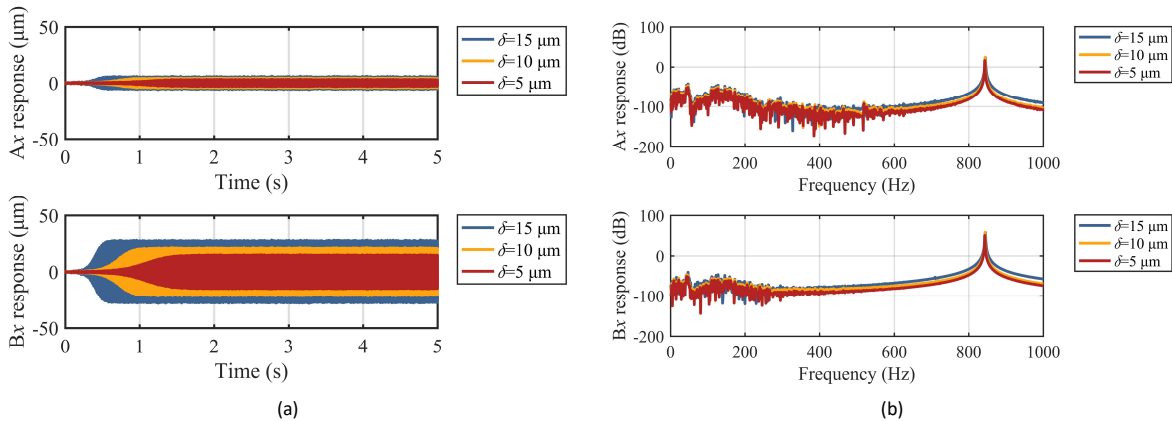
Figure 7   Comparison of dynamic responses in simulation (different interference) (a) Rotor time-domain responses (b) Rotor frequency-domain responses.
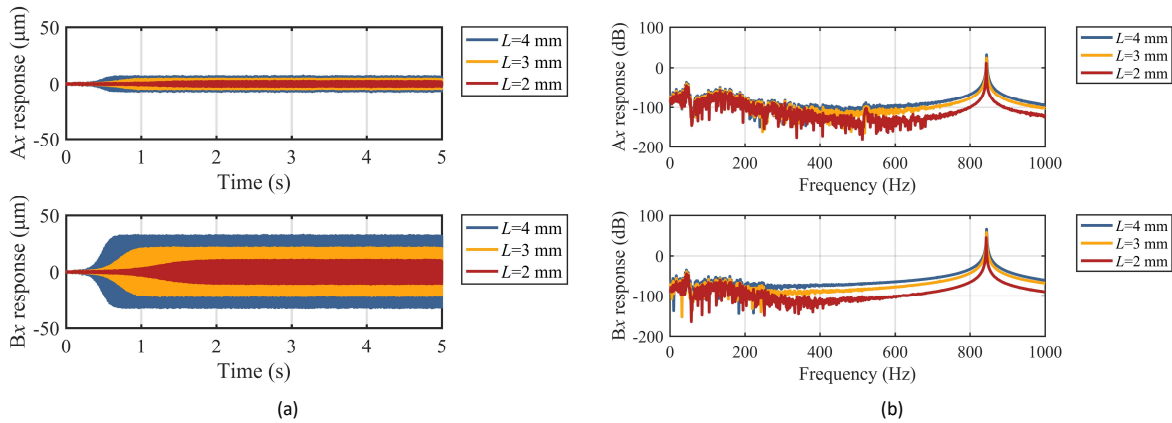
Figure 8   Comparison of dynamic responses in simulation (different contact length) (a) Rotor time-domain responses (b) Rotor frequency-domain responses.

4. Conclusions

This paper studies the perturbation caused by shrink fit interface contact in rotor-AMBs systems when the rotor is levitated without rotating by establishing the mechatronic rotor-AMBs model considering the interface contact. An additional stiffness matrix is introduced in order to characterize the interface contact between the rotor and the disk, and the value of the matrix is related to the contact stiffness and the contact length. Then the contact model for shrink-fit interfaces considering the multi-scale features of the rough contact surface is applied to calculate the contact stiffness under different interference and contact length. Finally, the influence of the interference and contact length on the dynamic characteristics of the system are numerically analyzed. Main conclusions of this study are summarized as follows:

(1) There is fluctuation in the rotor response when the rotor is levitated by AMBs because there is noise in the mechatronic system. When the disk is connected to the rotor by shrink fit, there is also multivariant slight vibration in the interface of shrink fit. The vibration energy caused by interface contact is acted upon the system in way of positive feedback and the resonance will be excited. The frequency of the 4th bending mode is higher than the cut-off frequency of the power amplifier and the controller is unable to control this mode due to the phase lag. As a result, the rotor vibrates at the frequency of the 4th bending mode.

(2) The normal and tangential stiffness increases with the increasing of interference and the increase of contact length.

(3) The steady vibration amplitude near the interface contact (AMB B) is greater than the amplitude on the other end (AMB A). The increase of the interference and the contact length will both increase the vibration amplitude.

References

Andras S and Flowers G (2007a) Suppression of internal damping-induced instability using adaptive techniques. ASME International Design Engineering Technical Conferences/Computers and Information in Engineering Conference, Las Vegas, USA, 4–7 September 2007, pp.1111-1118.
Andras S and Flowers G (2009b) Adaptive disturbance rejection and stabilization for rotor systems with internal damping. ASME International Design Engineering Technical Conferences/Computers and Information in Engineering Conference, San Diego, USA, 30 August–2 September 2009, pp.1063-1072.
Liu J, Ma C, Wang S, et al. (2019) Contact stiffness of spindle-tool holder based on fractal theory and multi-scale contact mechanics model. Mechanical Systems and Signal Processing 119: 363-379.
Schweitzer G and Maslen EH (2009) Magnetic Bearings: Theory, Design, and Application to Rotating Machinery. Heidelberg: Springer Berlin.
Smithanik J and Yannick P (2015) Applying API 617, 8th Edition to Expander-Compressors with Active Magnetic Bearings. In: 44th Turbomachinery & 31st Pump Symposium, Houston, USA, 14–17 September 2015, pp.349–364.
Sorge F (2013a) Approach to rotor-shaft hysteretic whirl using Krylov–Bogoliubov techniques. Journal of Vibration and Control 21(5): 883-895.
Sorge F (2014b) Nonlinear analysis of cylindrical and conical hysteretic whirl motions in rotor-dynamics. Journal of Sound and Vibration 333(20): 5042-5056.
Tan D, Chen J, Liao M, et al. (2014) Instability caused by cylindrical surface fit in rotor system. Mechanical Science and Technology for Aerospace Engineering 33(12): 1786-1790.
Wei T and Fang J (2008) Design of magnetically suspended elastic rotor notch filter based on two-frequency Bode diagram. Optics and Precision Engineering 16(5): 789-796.
Wu X, Jiao Y, Chen Z, et al. (2021) Establishment of a contact stiffness matrix and its effect on the dynamic behavior of rod-fastening rotor bearing system. Archive of Applied Mechanics 91(7): 3247-3271.
Xu Y, Zhou J, Di L, et al. (2015) Active magnetic bearing rotor model updating using resonance and mac error. Shock and Vibration 2015: 1-9.
Yukio I and Toshio Y (2012) Linear and Nonlinear Rotordynamics: A Modern Treatment with Applications. Hoboken: Wiley‑VCH Verlag GmbH & Co. KGaA.